

## Quantitative analysis of the heterogeneous population of endocytic vesicles

Konstantin Kozlov<sup>\*,§,¶</sup>, Vera Kosheverova<sup>†,¶,¶</sup>, Rimma Kamentseva<sup>†,||</sup>,  
 Marianna Kharchenko<sup>†,\*\*</sup>, Alena Sokolkova<sup>\*,††</sup>, Elena Kornilova<sup>†,‡,‡‡</sup> and  
 Maria Samsonova<sup>\*,§§</sup>

*\*Mathematical Biology and Bioinformatics Lab  
 Peter the Great St. Petersburg Polytechnic University  
 29, Polytechnicheskaya, St. Petersburg, 195251, Russia*

*†Institute of Cytology  
 RAS, 4, Tikhoretsky ave, St. Petersburg, 194164, Russia*

*‡St. Petersburg State University  
 7-9, Universitetskaya emb, St. Petersburg, 199034, Russia*

*§kozlov\_kn@spbstu.ru*

*¶vera77867@mail.ru*

*||rkamentseva@yandex.ru*

*\*\*mariasha2000@mail.ru*

*††alyonasok@yandex.ru*

*‡‡elena.kornilova@gmail.com*

*§§m.samsonova@spbstu.ru*

Received 5 October 2016

Revised 13 February 2017

Accepted 16 February 2017

Published 29 March 2017

The quantitative characterization of endocytic vesicles in images acquired with microscope is critically important for deciphering of endocytosis mechanisms. Image segmentation is the most important step of quantitative image analysis. In spite of availability of many segmentation methods, the accurate segmentation is challenging when the images are heterogeneous with respect to object shapes and signal intensities what is typical for images of endocytic vesicles. We present a Morphological reconstruction and Contrast mapping segmentation method (MrComas) for the segmentation of the endocytic vesicle population that copes with the heterogeneity in their shape and intensity. The method uses morphological opening and closing by reconstruction in the vicinity of local minima and maxima respectively thus creating the strong contrast between their basins of attraction. As a consequence, the intensity is flattened within the objects and their edges are enhanced. The method accurately recovered quantitative characteristics of synthetic images that preserve characteristic features of the endocytic vesicle population. In benchmarks and quantitative comparisons with two other popular segmentation methods, namely manual thresholding and Squash plugin, MrComas shows the best segmentation results on real biological images of EGFR (Epidermal Growth Factor Receptor)

§Corresponding author.

¶¶Equal contribution.

endocytosis. As a proof of feasibility, the method was applied to quantify the dynamical behavior of Early Endosomal Autoantigen 1 (EEA1)-positive endosome subpopulations during EGF-stimulated endocytosis.

*Keywords:* Image processing algorithm; image segmentation; colocalization; endocytosis.

## 1. Introduction

The populations of organelles and other subcellular structures within a cell have highly heterogeneous shape and content. At present, confocal scanning microscopy is one of the main tools for the analysis of intracellular processes. The quantitative image analysis is widely used to characterize the behavior of subcellular components, however, their heterogeneity complicates this task.

Challenges in quantitative characterization of subcellular structures can be easily illustrated through the analysis of Early Endosomal Autoantigen 1 (EEA1)-positive early endosomes and cargo-containing endocytic vesicles (for example, loaded with EGF-receptor complexes). Upon EGF binding to its specific receptor on the plasma membrane, the ligand-receptor complexes enter the cell within EGFR-containing transport vesicles during the process called receptor-mediated endocytosis and are then found in EEA1- and EGFR-positive structures. Formation of these structures means a series of fusions that result in cargo concentration, as well as in the alteration of the structures' number and size. An EEA1 was shown to mediate the first step of fusion.<sup>29</sup> EEA1 is believed to be recruited to the newly formed cargo-containing vesicles from the cytoplasm by binding with PI3P and Rab5, whose appearance on the membrane is triggered by activated EGFR.<sup>2,30</sup> However, EEA1 was demonstrated to be localized to vesicular structures not only after EGF stimulation, but also in the control (usually deprived for serum growth factors for at least several hours) cells.<sup>35</sup> EEA1-bearing endosomes are highly heterogeneous, in particular, individual endosomes may have quite different shape and amount of EEA1 protein. However, two subpopulations of EEA1-positive structures in the control cells can be distinguished, namely bright endosomes (usually large and localized in the juxtanuclear region of the cell) and dim ones, distributed more randomly throughout the cytoplasm.<sup>35</sup> Upon endocytosis stimulation, EEA1 and EGFR are detected in multidomain vesicular structures and their clusters, suggesting that EGFR-containing vesicles fuse with EEA1-positive endosomes but the two proteins in the common structure stay separated in specialized domains. It is not known what population of EEA1-positive structures, dim or bright, preferably mediates fusions with cargo-containing vesicles. Separate evaluation of parameters of interest for each of these early endosome subpopulations during the course of EGF-stimulated endocytosis could help to shed light on problem of their identity.

Image segmentation is the most critical step of quantitative image analysis. The aim of the procedure is to locate objects in the image by means of the so-called mask image in which white pixels mark the objects and black ones correspond to the background. In the case of blurred object in low contrast images, the segmentation

causes a number of challenging problems,<sup>6,23,31</sup> such as the exclusion of dim objects, overestimation of bright objects sizes, erroneous gluing together of closely localized objects, etc.

Up to now, numerous software platforms and automated methods for image segmentation have been developed.<sup>13</sup> Popular adaptive model-based approaches such as geodesic active contours,<sup>5</sup> graph-cut-based algorithms<sup>4</sup> and their combinations<sup>34</sup> typically work well only when the intensity distributions of regions of interest and the background are well distinguishable. A method based on active contours and wavelet transform specifically designed for efficient endosome extraction was developed in Ref. 11 and implemented in Icy software.<sup>10</sup> An approach based on multi-parametric fitting of image intensity by powered Lorentzian<sup>25</sup> was investigated in Ref. 7. Another model-based approach was proposed in Ref. 1. Unfortunately, while being extremely powerful, these methods process only one image color channel at a time, and, therefore, may underestimate the sizes of complex objects labeled with several fluorescent stains. Using different global threshold methods, such as Otsu threshold,<sup>22</sup> the Ridler and Calvard<sup>24</sup> method or manual thresholding, based on the maximal visual agreement between the original and segmented images, for the processing of low contrast images also leads to under- or over-estimation of the object sizes. Local threshold methods, in turn, are sensitive to noise and are also not always appropriate.

The accurate detection of colocalization of fluorescently labeled objects is important for analysis of endocytosis as this complex process involves the dynamic interactions of endosomes with different incoming vesicles and vesicle carriers targeted to distinct organelles, as well as association of endosomes with proteins from cytosol.<sup>8</sup> Currently, two main approaches are applied to estimate colocalization of objects in different color channels. The object-based methods firstly use segmentation to detect objects and after that, quantify their spatial overlap. Needless to say the performance of these methods critically depends on the segmentation accuracy. Along with object-based methods, the pixel-wise colocalization analysis is also applied to detect object colocalization. These methods estimate an overlap between the pixel intensities of different color channels by calculating Manders' and Pearson correlation coefficients and may not be suitable for colocalization studies involving objects with different fluorescent intensity. Therefore, the majority of colocalization problems demand customized solutions.<sup>12</sup>

Here, we present a Morphological reconstruction and Contrast mapping segmentation method, called MrComas, for the segmentation of the endocytic structures population that copes with the heterogeneity in their shape and intensity. The contrast mapping is based on the idea of using a dilation process near a local maximum and an erosion process around a local minimum to create a "shock" between the basins of attraction of the intensity local extrema for edge enhancement.<sup>18</sup> The attractive properties of the shock filters are the creation of the strong discontinuities at the object edges and the flattened signal within regions.<sup>28,32</sup>

We demonstrate the applicability and performance of MrComas on synthetic images preserving characteristic features of the EEA1-bearing endosomes, as well as on real experimental data on EGF receptor-mediated endocytosis. We show that the method outperforms the segmentation methods implemented in ImageJ, namely Squash plugin and manual thresholding. Finally, as the identity of two subpopulations of the EEA1-positive endosomes is not clear so far, we apply MrComas to quantitatively characterize their dynamical behavior during EGF stimulated endocytosis.

## 2. Experimental Design

**Stimulation of EGFR endocytosis.** HeLa cells (Russian Cell Culture Collection, Institute of Cytology RAS) were grown on  $10 \times 10$  mm coverslips to achieve about 70% monolayer at the day of experiment. The cells were serum-starved in DMEM containing 0.1% serum for 12 h before experiment. The EGF receptor endocytosis was stimulated according to pulse-chase protocol. Briefly, the cells were washed twice with warm ( $37^{\circ}\text{C}$ ) working medium (WM) consisting of DMEM supplemented with 20 mM HEPES and 1% BSA. Endocytosis was stimulated by addition of 40 ng/mL EGF (Sigma-Aldrich, USA) in fresh WM at  $37^{\circ}\text{C}$  for 5 min. The unbound ligand was washed out with WM and, incubation in WM was continued at  $37^{\circ}\text{C}$  and for indicated time.

**Immunofluorescent staining of EEA1 and EGFR.** At the indicated time, after stimulation, the cells were fixed with freshly prepared 4% formalin for 15 min at room temperature (RT) and washed with PBS for 5 min. Then, the cells were permeabilized with 0.5% Triton X-100 for 15 min at RT and, after washing with PBS, were incubated in 1% BSA for 30 min at RT to block unspecific antibody binding. After that, primary antigen-specific antibodies diluted in 1% BSA were added to the cells. The cells were incubated with polyclonal rabbit antibody raised against the intracellular domain of EGFR (Cat. #2232, Cell Signaling, USA) in dilution 1:100 overnight at  $4^{\circ}\text{C}$  and consequently with monoclonal mouse antibody specific to EEA1 (Cat. # 610457, Transduction Lab, USA) in dilution 1:200 for 1 h at RT. Then the cells were washed with PBS containing 0.1% Tween-20 (BioRad, USA) and were incubated with secondary antibodies GAR-Alexa Fluor 568 (Molecular Probes, USA) and GAM-Alexa Fluor 488 (Molecular Probes, USA), respectively, in dilution 1:200 for 20 min at  $37^{\circ}\text{C}$ . Finally, the cells were mounted in 0.2 M DABCO (1,4-diazabicyclo(2.2.2) octane) (Sigma-Aldrich, USA) glycerol-containing media.

**Image acquisition.** Images were obtained using Leica TCS SP5 confocal microscope (Leica Microsystems, Germany) with  $100\times$  oil objective ( $\text{NA} = 1.3$ ). Series of optical sections (z-stacks) were collected with  $0.5\text{ }\mu\text{m}$  step. The image size was  $1024 \times 1024$  pixels with the gray scale resolution 8 bit. The red and green channels corresponded to EGFR and EEA1 signals respectively. Experimental images of 10–13 cells were obtained for control group and each of three time moments, namely

15, 30 and 60 min after stimulation. For imaging, we selected cells with a typical interphase phenotype. A full-size representative image is shown in Fig. S3.

### 3. MrComas Algorithm

**Overview.** The MrComas algorithm processes both channels simultaneously and consists of five major steps (Fig. 1). Firstly, it accepts several biologically-relevant parameters for input images. Instead of taking probabilistic approach to parameter estimation<sup>1,7</sup> that may raise the computational costs of processing, the reasonable defaults are provided for these parameters, as detailed below in paragraph *Input parameters definition* (step 1, see Fig. 1). Next, contrast enhancement and denoising of input images are performed (Fig. 1, step 2). Then, the images are enlarged by the factor of four with the nearest neighbor algorithm to enhance the quality of subsequent steps and segmented. Both closing and opening by morphological reconstruction<sup>33</sup> are computed. Subsequently, the contrast mapping operator takes maximum between the difference and the pixel-by-pixel product of reconstructed images and produces the rough mask for each channel (Fig. 1, step 3). At the fourth step, the distance transform followed by the watershed transform<sup>20</sup> are applied to the combined mask of both channels to split the erroneously merged objects. These procedures result in the object mask and the intersection of this mask with rough masks constructed at the preceding step provides the channel masks. The quality of segmentation can be assessed visually by inspection of the object borders overlaid with the original image. Finally, the masks are brought to the original size and the quantitative measurements are performed (Fig. 1, step 5). The MrComas is implemented in the framework of previously developed tool ProStack<sup>17</sup> but can be used as a standalone application with graphical user interface (see Fig. S1). It consists of about a 100 elementary operations. The individual steps are explained in the following sections. MrComas is free and open source software available at <http://sourceforge.net/p/prostack/wiki/mrcomas>.

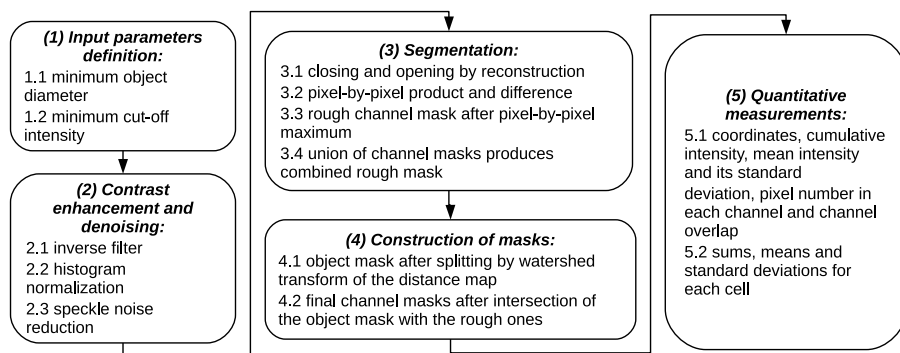


Fig. 1. Flowchart of MrComas algorithm.

**Input parameters definition (step 1, see Fig. 1).** The biologically-relevant parameters of MrComas, namely the minimal diameters (in pixels) of objects in red and green channels (point 1.1, Fig. 1) and minimal cut off intensities (point 1.2) can be set interactively via the graphical user interface (see Fig. S1). The reasonable defaults are provided for the algorithmic parameters which may also be adjusted for individual images at different time points. One of the parameters makes it possible to distinguish and separately analyze dim and bright vesicles in green channel.

**Contrast enhancement and denoising (step 2).** The input images are inversely filtered (2.1) and the histogram is normalized to enhance the contrast (2.2). To assist further processing, it is desirable to reduce speckle noise in images (2.3) by the Crimmins Complementary Hulling algorithm in which the amount of the speckle noise present in the image is measured as the ratio of noise deviation to its mean.<sup>9</sup>

**Segmentation (step 3).** At the next step, the images are enlarged by the factor of four. In the following, an image  $I$  is a mapping from a finite rectangular subset  $L$  of the discrete plane  $Z^2$  into a discrete set  $0, 1, \dots, N - 1$  of gray-levels. Let the dilation  $\delta_B$  and erosion  $\epsilon_B$  by structural element  $B$  be defined as:

$$\delta_B(I) = \bigvee_{y \in B} I(y) = I \oplus B \quad \epsilon_B(I) = \bigwedge_{y \in B} I(y) = I \ominus B$$

where  $\wedge$  and  $\vee$  denote infimum and supremum respectively. Then formulae

$$\delta_{I,B}^1(J) = (J \oplus B) \wedge I \quad \epsilon_{I,B}^1(J) = (J \ominus B) \vee I$$

denote geodesic dilation  $\delta_{I,B}^1$  and erosion  $\epsilon_{I,B}^1$ . Binary reconstruction extracts those connected components of the mask image which are marked in the marker image, likewise, in grayscale, it extracts the peaks of the mask image which are marked by the marker image.<sup>33</sup> Usage of the dilated mask image  $I$  as the marker  $J$ :  $J = \delta_B(I)$  defines closing by reconstruction:

$$\gamma_B(I) = \epsilon_{I,B}^1 \epsilon_{I,B}^1 \dots \epsilon_{I,B}^1 [\delta_B(I)].$$

Opening by reconstruction (3.1) uses eroded mask  $I$  as a marker  $J$ :  $J = \epsilon_B(I)$ :

$$\phi_B(I) = \delta_{I,B}^1 \delta_{I,B}^1 \dots \delta_{I,B}^1 [\epsilon_B(I)].$$

Then the difference between closing and opening by reconstruction (3.2) has the meaning of the gradient:

$$\nabla_B(I) = \gamma_B(I) - \phi_B(I).$$

To create strong discontinuities at object edges and flatten signal within the objects, the contrast mapping operator takes maximum between the difference and the pixel-by-pixel product of reconstructed images and produces the rough mask (3.3) for each channel:

$$R = \max\{\nabla_B(I), \gamma_B(I) \odot \phi_B(I)\}.$$

**Construction of masks (step 4).** The combined rough mask of both channels (3.4) is subjected to the distance transform followed by the watershed transform<sup>20</sup> to split the erroneously merged objects (4.1). The resulting object mask is overlapped with rough channel masks to produce the final masks for the channels (4.2). The object borders are overlaid over the original image to visually assess the quality of segmentation.

**Quantitative measurements (step 5).** The quantitative information, namely coordinates, cumulative intensity, mean intensity and its standard deviation, pixel number in each channel and channel overlap, is extracted for each object (5.1) and stored as a table in the CSV format. The sums, means and standard deviations of all these quantities are then calculated for each cell (5.2) over all objects and for each time point over all cells.

#### 4. Performance Evaluation

**Synthetic images.** The set of synthetic images for red and green channels was generated using the object masks for these channels constructed from real images for time point 30 min after endocytosis stimulation. The intensity for all pixels in the object was set to maximal value of the real image pixels. Imaging was simulated by adding background intensity equal to 1 and subsequent convolution of the objects with the Gaussian to simulate the PSF of the experimental setup. The mean and variance of the Gaussian were set to pixel intensity and to 1 respectively.

Noisy images were then obtained by adding the Poisson-distributed noise. In order to control the noise level in synthetic images, we transformed the image intensities  $I$  to expected photon counts  $k$  using the linear function  $k(i, j) = gI(i, j)$  where the gain  $g$  is the control parameter. A new value for each pixel  $(i, j)$  was sampled from the Poisson distribution with parameter  $k(i, j)$  and transformed back to gray-scale intensity. By varying the gain value  $g$ , we adjusted the peak signal-to-noise ratio (pSNR) in the range of 6–30.<sup>14</sup> For each  $g$  value and each of the  $N = 12$  masked images, one sample image was generated. In this way, the generated images retain the heterogeneity of object shapes and intensities intrinsic to the source images.

The dependence of pSNR on the gain in synthetic images is shown in Figs. 2(a) and 2(b) for red and green channels respectively. As indicated in the figures, at gain values 30 and 50, the pSNR value is close to 30, the value found in source images.

**Colocalization measurements.** The colocalization was studied by calculating Manders' coefficients<sup>19</sup>  $M_1$  and  $M_2$  according to the following formulae:

$$M_1 = \frac{\sum_i A_i(B_i > 0)}{\sum_i A_i} \quad M_2 = \frac{\sum_i B_i(A_i > 0)}{\sum_i B_i} \quad (1)$$

where  $A_i$  and  $B_i$  are intensities of the pixel  $i$  in channels  $A$  (red channel) and  $B$  (green channel) respectively.

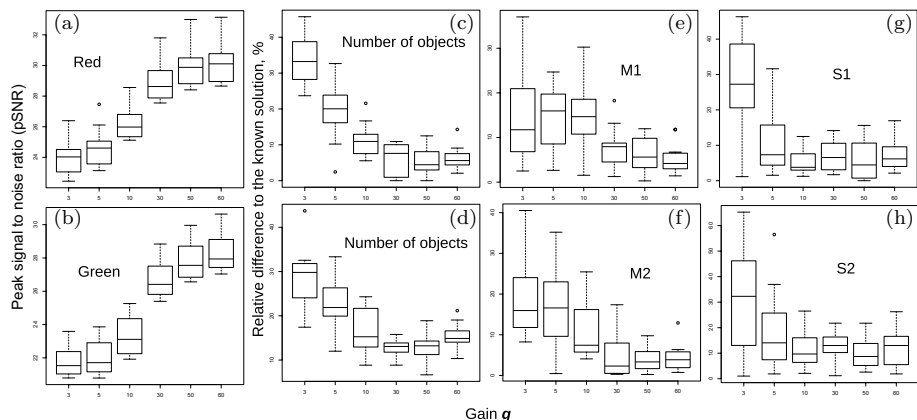


Fig. 2. The performance evaluation on synthetic images. Upper and bottom rows present graphs for red and green channels respectively. The dependence of pSNR (peak signal-to-noise ratio) (a)–(b) and three error estimators (c)–(h) on gain. Dependence graphs for relative differences to the known solutions in the number of objects (c),(d), Manders’ coefficients (e),(f), fraction of overlapping area in vesicles (g), (h). All error estimators attain minimum at gain values higher than 30, for which the pSNR is close to the value measured in experimental images.

We also calculated the fraction of colocalized vesicles  $N_j$  and the fraction  $S_j$  of the total area occupied by objects in one channel that overlap with objects in the other channel (fraction of overlapping area),  $j = 1, 2$ :

$$N_1 = \frac{N_A(B > 0)}{N_A} \quad N_2 = \frac{N_B(A > 0)}{N_B} \quad (2)$$

$$S_1 = \frac{S_A(B > 0)}{S_A} \quad S_2 = \frac{S_B(A > 0)}{S_B} \quad (3)$$

where  $N_\bullet$  is the number of vesicles in corresponding channel and  $S_\bullet$  is the area in pixels occupied by objects.

**Other software tools.** To compare MrComas method with other popular segmentation methods, we used the open source software ImageJ 1.49p.<sup>27</sup> The images were spatially calibrated with the “Set Scale” function. To generate a binary mask, an image underwent gray level thresholding and the threshold value was selected manually to maximize visual correspondence between the original and binarized image. The number, mean area and mean intensity of the EEA1- and EGFR-containing structures were calculated using the “Analyze Particles” function.

To compare the object masks, we also used Squash plugin<sup>26</sup> with algorithmic settings selected to balance detection power and sensitivity to noise. The Manders’ coefficients  $M_1$  and  $M_2$  were evaluated using JACoP plugin.<sup>3</sup>

To validate the significance of differences in segmentation method performance, as well as in dynamical behavior of the EEA1-positive endosome subpopulations, we performed Student’s two tailed  $t$ -test for independent samples.



## 5. Results and Discussion

### 5.1. Performance on synthetic images

To quantitatively characterize the performance of the MrComas algorithm, we generated a set of synthetic images that preserve the heterogeneity in object shapes and signal intensities intrinsic to the source images of the EGFR endocytosis. For each of the source images, we know number of objects, the values of both Manders' coefficients  $M_1$  and  $M_2$  (1), as well as the values of  $S_1$  and  $S_2$  (3) coefficients (see *Colocalization measurements* section).

We defined the following error estimators to measure MrComas performance. The relative difference between the number of detected objects in synthetic and source images evaluate the quality of segmentation. The relative difference in the values of the Manders' coefficient  $M_1$  ( $M_2$ ) as well as the relative difference in the values of  $S_1$  ( $S_2$ ) coefficient helps to assess the accuracy of colocalization analysis.

The dependence of these error estimators on the gain is presented in Fig. 2, panels C, E, G and D, F, H, for red and green channels respectively. The average percent of lost objects for red (EGFR) and green (EEA1) channels was as low as  $5.4 \pm 3.6\%$  and  $12.8 \pm 1.8\%$  respectively. The slightly higher segmentation error obtained for green channel can be attributed to the larger heterogeneity of the population of EEA1-bearing endosomes in comparison with that of EGFR-positive vesicles. The relative difference in the values of the Manders' coefficients  $M_1$  and  $M_2$  was  $6.2 \pm 4.0\%$  and  $3.9 \pm 2.9\%$  and in the values of  $S_1$  and  $S_2$  coefficients  $6.9 \pm 4.3\%$  and  $9.7 \pm 5.9\%$  respectively. The noteworthy details are that for each estimator, the minimal error value was attained at gains 30 and 50 with statistically insignificant difference ( $P > 0.05$ ) and that the pSNR (peak signal-to-noise ratio) values for these gains are close to those in source images.

Varying the settings for the Squash method, we obtained the minimal value of 30% lost objects which is insufficiently high. This could be accounted for the fact that for correct image segmentation, the information from both channels should be combined at the mask construction step, while the Squash method treats each channel separately.

### 5.2. Comparison of MrComas with other segmentation methods

Next, we applied MrComas to real biological images of EGFR endocytosis to test the method accuracy in comparison with other popular segmentation methods, namely manual thresholding (MT) and Squash plugin both implemented in commonly used open source software ImageJ.<sup>27</sup> The images present HeLa cells at 15, 30 and 60 min after endocytosis stimulation with EGF, as well as control unstimulated cells (see representative images in Fig. S2). The cells were stained with fluorescently labeled antibodies to monitor the dynamical behavior of EEA1-and EGFR-bearing structures. For each time point and control, we analyzed 10–13 images of individual cells.

The images were collected as series of optical sections and, after acquisition, the stacks were reduced to single images by maximum projection.

It is well known that segmentation is challenging when the objects in the image are heterogeneous with respect to signal intensity and shape. The images of EEA1-bearing endosomes are an excellent example of such images. Indeed, the early endosomes have quite different shape and amount of EEA1 protein and evidently form two subpopulations of dim and bright structures within the cell. Hence, the images of EEA1-positive endosomes seem to be the perfect choice to illustrate and compare the segmentation performance of MrComas and other algorithms. Figure 3(a) presents two  $160 \times 160$  pixels crops enlarged for better mask presentation, that show the small regions of the typical unstimulated control cell and the cell after 30 min of EGF stimulation, labeled with anti-EEA1 antibodies, as well as the

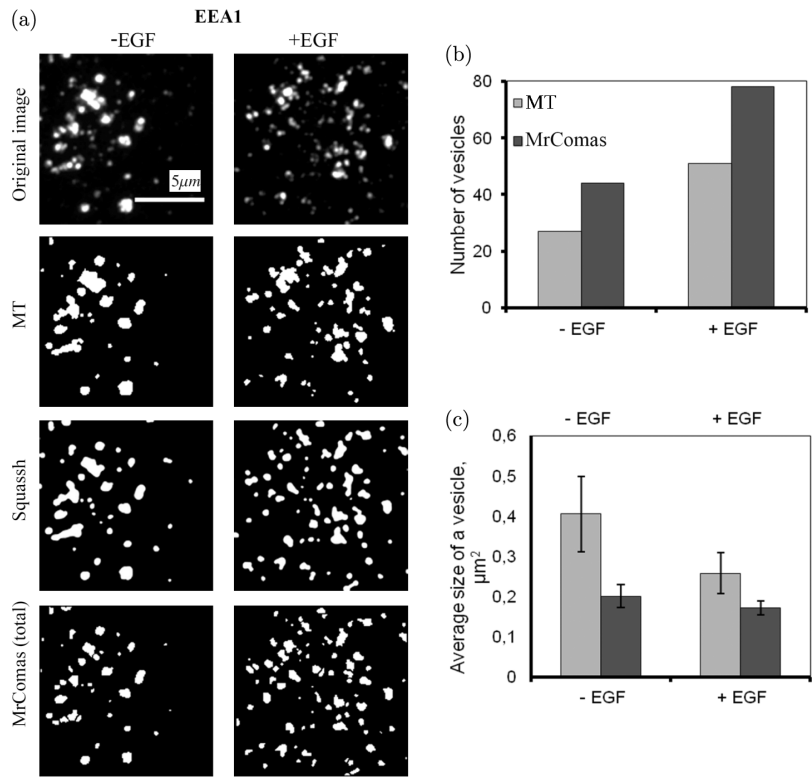


Fig. 3. The result of segmentation of images of the EEA1-bearing endosomes in unstimulated control cells (left column) and cells after 30 min of EGF stimulation (right column). Rows from top to bottom: original images, segmentation results for manual thresholding (MT, threshold value was 36 and 29-pixel intensity for control and 30 min-stimulated cells, correspondingly), Squash and MrComas. The original images are  $160 \times 160$  maximal projections' crops, representing the enlarged region of typical cell, scale bar is  $5 \mu\text{m}$ . Number (b) and average size (c) of EEA1-positive endosomes are calculated to compare segmentation performance of MT and MrComas. Note that the number of structures in these demonstrative crops does not correlate with total number of the structures per a whole cell.

binary masks of these crops constructed with MrComas, manual thresholding (MT, threshold value was 36 and 29-pixel intensity for control and 30 min-stimulated cells, correspondingly) and Squash with regularization weight experimentally set to 0.15. It is evident that MrComas provides the best segmentation result. The bright EEA1-endosomes are accurately isolated from the rest of the image and their sizes in the mask differ little from those in original image. It is also noteworthy that the number of falsely combined objects in the mask is small (Fig. 3(a)). In comparison with manual thresholding, MrComas detects larger number of dim EEA1-positive endosomes (Figs. 3(a), (b), the average area of detected endosomes being smaller (Fig. 3(c)). The estimated value of  $\approx 0.2 \mu\text{m}^2$  largely agrees with the measurements done by Ref. 16. In this work, it was demonstrated that the majority of EEA1-positive endosomes have diameter in the range of  $0.4\text{--}0.8 \mu\text{m}$  with the average diameter  $0.5 \mu\text{m}$ . However, it is worthy to note that the genuine endosome size still cannot be evaluated using fluorescent microscopy.

Note that the masks obtained with the state-of-the-art Squash algorithm<sup>26</sup> and manual thresholding contain similar errors, in particular, bright EEA1-positive endosomes are moderately enlarged and in some cases glued together, while the dim EEA1-positive endosomes are partially lost (Fig. 3(a)). Consequently, we used the results of manual thresholding for further comparison.

To continue the method comparison, we quantify the dynamics of vesicle number and average area upon EGF stimulation. Though EGFR-positive vesicles are relatively homogeneous with respect to intensity at any endocytosis time point, the segmentation of these objects with manual thresholding is error-prone. Indeed, as it is evident from Fig. S2, the sizes of the EGFR-positive vesicles in the masks created with manual thresholding are overestimated. In general, the average size of the vesicle area calculated by MrComas tends to be smaller in comparison to manual thresholding (Fig. 4(b)). Irrespective of segmentation algorithm, the number of EGFR-containing vesicles is large at 15–30 min after endocytosis stimulation (Fig. 4(a)) and significantly decreases in 60 min-stimulated cells ( $P = 0.006$  and  $P = 1.41 \times 10^{-6}$  for MT and MrComas respectively), that reflects the EGFR degradation in lysosomes at late stages of endocytosis.<sup>15</sup> It is important that while the average size of EGFR-vesicles measured by MT remains relatively constant, to the contrary, quantification by MrComas demonstrates significant reduction of vesicle sizes in the course of endocytosis (Fig. 4(b)), that is in line with the concept of endosome maturation from early endosomes to the late ones.<sup>21</sup> Briefly, when an endosome matures, after series of fusions occurring during the first 5–20 min of endocytosis, the portions of its membrane invaginate and pinches off into the endosome lumen resulting in the formation of multivesicular bodies. As the result, the endosome size is reduced, but the EGFR concentration (and fluorescence intensity) per vesicle increases, that, as we suppose, led to the overestimation of the EGFR-positive vesicle sizes by MT (Fig. 4(b)). The denoising algorithm applied on step 2 of MrComas removes faulty intensity spots thus correcting the number of vesicles. Further, combination of contrast enhancement and contrast mapping operations

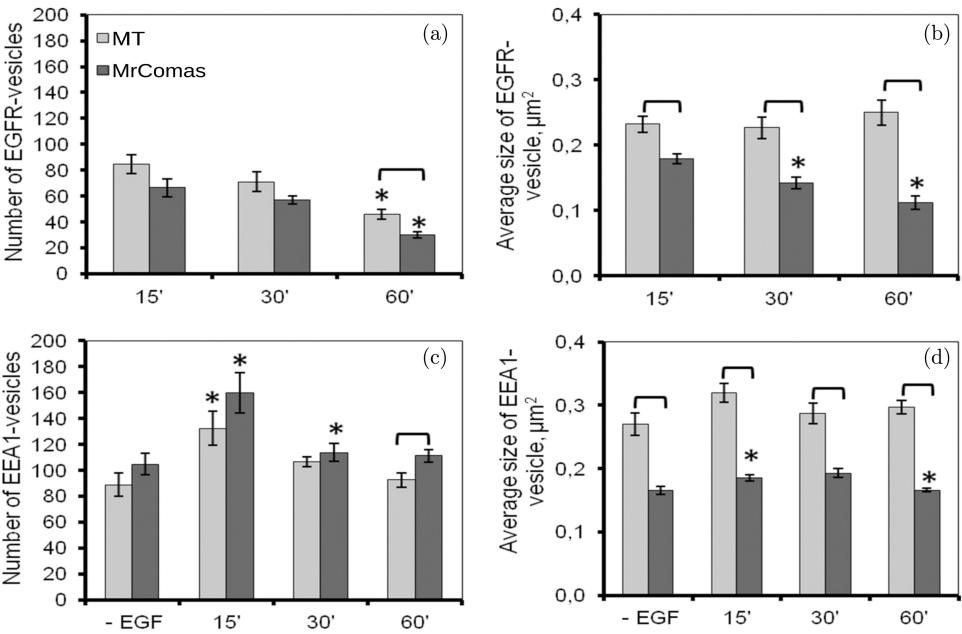


Fig. 4. The comparison of segmentation performance of MrComas and manual thresholding. The dynamics of quantitative properties, namely vesicle number (a), (c) and average size (b), (d) for EGFR- and EEA1-positive structures, respectively, was evaluated in unstimulated cells and at 15, 30 and 60 min after endocytosis stimulation with EGF. Brackets mark statistically the significant differences in the quantitative properties of vesicles segmented with MrComas or manual thresholding (MT). Asterisks denote statistically the significant difference between a quantitative property at a given and preceding time points and for vesicles segmented with the same method. For each time point and control, we analyzed 10–13 images of individual cells.

sharpens the borders of objects and consequently facilitates a more precise estimation of vesicle sizes.

We further analyzed the dynamics of the EEA1-bearing endosome number and average area in EGF stimulated cells. As it is evident from Figs. 4(c), 4(d) the reduction of these quantities was only observed when MrComas was applied to segment images, the endosome number and the average area in images segmented with MT (Figs. 4(c), 4(d)) being nearly constant that is not consistent with known facts.

### 5.3. Quantitative analysis of the EEA1-positive endosome subpopulations

To demonstrate the suitability of MrComas for analysis of real biological problems, we applied this method to quantify the dynamical behavior of EEA1-positive endosome population during EGF-stimulated endocytosis. As it is illustrated in Fig. 5(a) MrComas accurately isolates endosomes of different signal intensity that

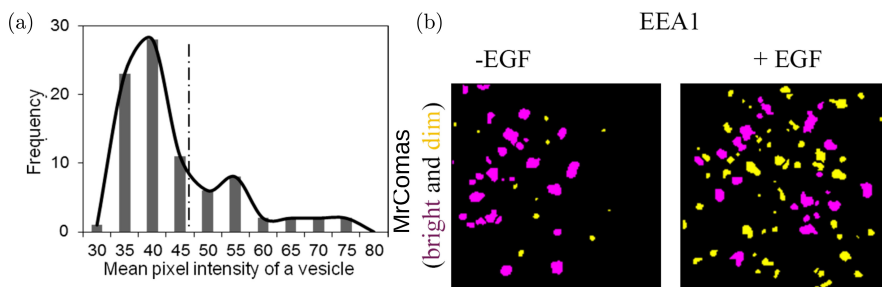


Fig. 5. The partition of the total EEA1-positive endosome population into two subpopulations of bright and dim structures (a) The distribution of EEA1-positive endosomes according to their mean pixel intensity in an one representative unstimulated cell. The histogram and approximating curve are plotted. Dotted line shows threshold value used to distinguish bright and dim structures; (b) Masks of bright (magenta) and dim (yellow) EEA1-positive structures constructed from images presented in Fig. 3.

makes it possible to specify a threshold value for mean signal intensity and subdivide the whole endosome population into two subpopulations of bright and dim structures (Fig. 5(b)).

We found that the behavior of the two subpopulations after endocytosis stimulation is different. For example, the number of dim structures exceeds the number of bright ones more than two-fold at any endocytosis time point. The largest number of both bright and dim structures is observed at 15 min after endocytosis stimulation (Fig. 6(a)). In respect to the average endosome size, this quantity does not change in case of bright endosomes, however the average size of dim endosomes first increases, reaches maximum value at 30 min and then decreases (Fig. 6(b)). These changes most probably reflect the fissions and fusions of endosomes.

Next, we studied the colocalization of the EGFR-positive vesicles with dim and bright EEA1-positive endosomes. We used the same series of images as above with small modification, namely instead of maximal projection, we analyzed a single optical section of z-stack series selected at the basal part of a cell where the majority of endosomes is localized. Firstly, we calculated Manders' overlap coefficients, which are good indicators of colocalization events in two-dimensional images. We found that at any endocytosis time point, the value of  $M_1$  coefficient exceeds that of  $M_2$  coefficient for both subpopulations (Figs. 6(c), 6(d)). The reasonable explanation is that the number of EGFR-bearing vesicles (detected in red channel) is lower than that of EEA1-positive endosomes (detected in green channel), so only part of the EEA1-positive endosomes population is involved in interactions with EGFR-containing vesicles. Moreover, EEA1 and EGFR signals may be localized in neighboring domains of one structure with minimum overlapping area that additionally decreases both coefficient values. Such overlap pattern is not the result of chromatic shift because relative orientation of EEA1 and EGFR signals differs from structure to structure within one image. However, we did not reveal any significant differences in the Manders' coefficient values between bright and dim subpopulations (Figs. 6(c),

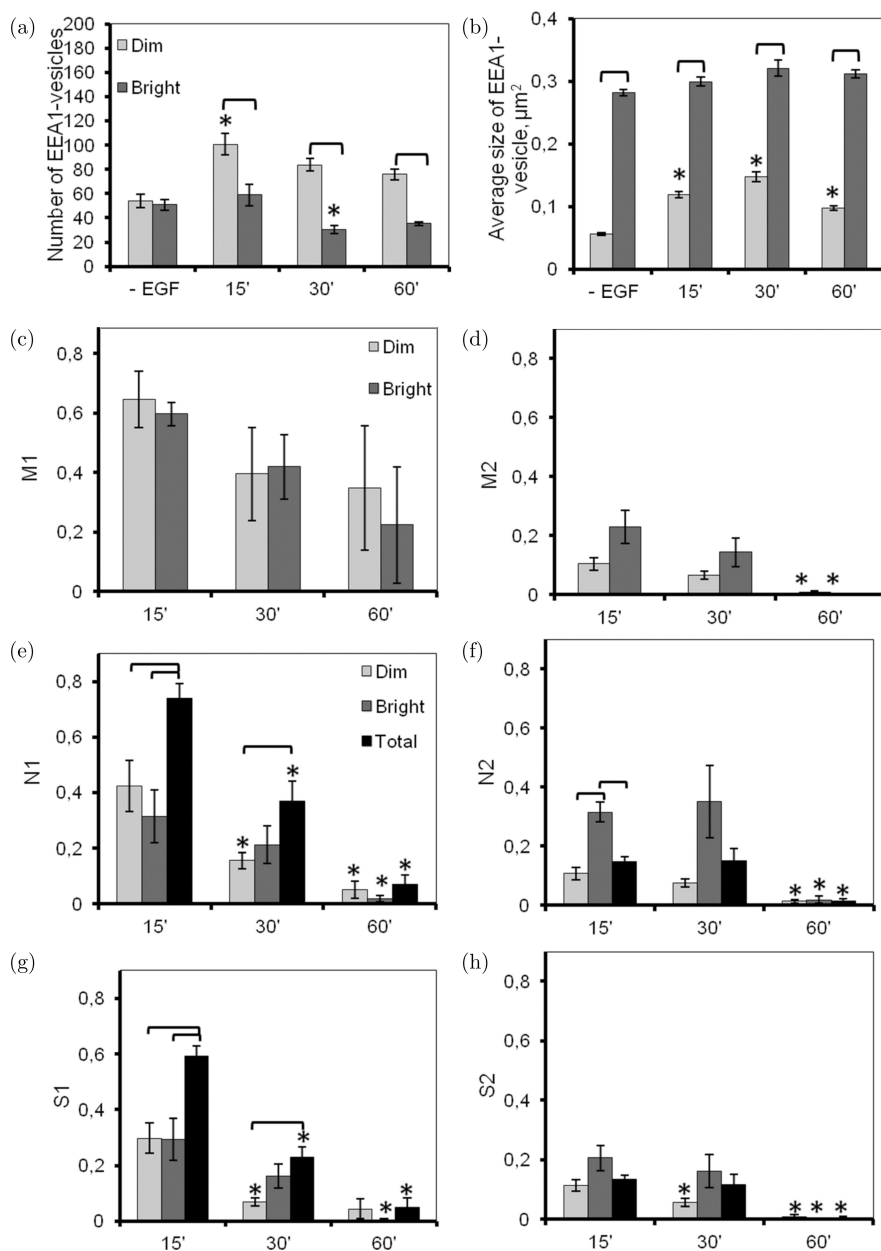


Fig. 6. The dynamic behavior of the EEA1-positive endosome subpopulations during EGFR endocytosis. Number (a) and average size (b), Manders' coefficients  $M_1$  (c) and  $M_2$  (d), coefficients  $N_1$  (e),  $N_2$  (f),  $S_1$  (g),  $S_2$  (h) for total, dim and bright EEA1-positive structures were calculated using MrComas. Brackets mark statistically significant differences in quantitative properties of endosomes from different subpopulations. For each subpopulation, asterisks denote statistically significant difference between a quantitative property at a given and preceding time points.

6(d)) that was reasonable to expect as Manders' coefficients calculate the relative sum of pixel intensities of the signal in one channel coincident with a signal in the other channel and therefore may not be appropriate for measuring colocalization of objects in endosome subpopulations heterogeneous with respect to signal intensity inside individual masks.

Thus, we used the object-based approach to evaluate the colocalization events in subpopulations. To that end, we calculated the fraction of dim and bright EEA1-positive endosomes colocalizing with EGFR-positive endosomes ( $N_2$  coefficient, Fig. 6(f)), the fraction of area occupied by dim and bright EEA1-positive endosomes overlapping with EGFR-vesicles ( $S_2$  coefficient, Fig. 6(h)), the fraction of EGFR-vesicles colocalizing with dim or bright EEA1-positive endosomes ( $N_1$  coefficient, Fig. 6(e)) and the fraction of area occupied by EGFR-containing vesicles overlapping with dim or bright EEA1-positive endosomes ( $S_1$  coefficient, Fig. 6(g)). As it is evident from Fig. 6(e) and 6(g), the values of both  $N_1$  and  $S_1$  coefficients for dim endosomes are high at 15 min, but significantly decrease by 30 min after stimulation of endocytosis ( $P = 0.025$  for  $N_1$ ,  $P = 0.003$  for  $S_1$ ). Contrary to dim endosomes, the values of  $N_1$  and  $S_1$  coefficients for bright endosomes do not change with time, indicating that the interaction of these endosomes with EGFR-positive vesicles is apparently of longer duration as compared to interaction of dim EEA1-positive endosomes. At 15 min after onset of endocytosis, the value of  $N_2$  coefficient for bright endosome subpopulation is larger than for dim one (Fig. 6(f)), suggesting that EGFR-positive vesicles are preferably colocalized with bright EEA1-positive endosomes.

## 6. Conclusions

The segmentation of images heterogeneous with respect to object shapes and signal intensities is a difficult task that often involves errors such as loss of dim objects, overestimation of bright objects sizes and erroneous gluing together of closely localized objects. The images of endocytic structures participating in the process of receptor-mediated endocytosis are the classical example of images of this kind. We developed a segmentation method, called MrComas for the segmentation of the early endosome population that copes with the heterogeneity in their shape and intensity. The method employs morphological opening and closing by reconstruction in the vicinity of local minima and maxima respectively thus creating the strong contrast between their basins of attraction. As a consequence, the intensity is flattened within the objects and their edges are enhanced.

To quantitatively characterize the performance of the MrComas algorithm, we generated a set of synthetic images that preserve the level of heterogeneity inherent to the images of fluorescently labelled endocytic structures. For these images, the mean segmentation error is about 10% with a slightly higher value for heterogeneous population of endosomes in green channel. Compared with two other popular segmentation methods, namely manual thresholding and Squash, MrComas shows the

best segmentation results on both synthetic images and real biological images of EGF-stimulated endocytosis. It accurately isolates objects and provides good quality of segmentation for all levels of signal intensities. As a result, the dynamics of vesicle number and sizes during EGF stimulated endocytosis is in good agreement with known facts about endosome maturation only in images segmented by MrComas.

The performed numerical experiments showed that, though the building blocks of MrComas are not new, the proposed combination of contrast enhancement and contrast mapping operations together with coordinated processing of two color channels determine the advantages of developed method.

The excellent performance of the MrComas method opens access to further analysis of segmented images. Here, we studied the colocalization between endocytic structures detected in different color channels. Firstly, we demonstrated that for synthetic images, the error in the values of coefficients used to measure colocalization does not exceed 10%. Next, we analyzed the real biological images of EGF stimulated endocytosis to quantitatively characterize the colocalization of the EGFR-positive vesicles with dim and bright EEA1-positive endosomes. As the value of the  $M_1$  Manders' coefficient exceeded that of  $M_2$  coefficient for both subpopulations and at any endocytosis time point, we drew a conclusion that the number of EEA1-positive endosomes are in excess and therefore only part of the EEA1-positive endosome population is involved in interactions with EGFR. However, we did not reveal any significant differences in the Manders' coefficient values between bright and dim subpopulations. The most reasonable explanation for this result is the observed high cell to cell variation in Manders' coefficient values (see error bars in Figs. 6(c), 6(d)) that resulted from highly variable intensities of both EGFR- and EEA1-positive structures.

Therefore, the object-based approach was used to evaluate the colocalization events in subpopulations. It turned out that contrary to bright EEA1-positive endosomes, the values of both  $N_1$  and  $S_1$  coefficients for dim endosomes (Figs. 6(e), 6(g)) decrease with time and that vice versa at the onset of endocytosis the value of  $N_2$  coefficient for bright endosome population is larger than that for dim one (Fig. 6(f)). These results demonstrate that the bright EEA1-positive endosome interact with EGFR-positive vesicles for a longer period of time in comparison with dim EEA1-positive endosomes. Moreover, the EGFR-positive vesicles are preferably colocalized with bright EEA1-positive endosomes.

Our results support the hypothesis that dim and bright EEA1-positive endosomes are functionally different that, nevertheless, should be subsequently proven in experiment. We propose that bright EEA1-positive endosomes may undergo fissions to generate dim ones, as well as dim endosomes are able to fuse with each other and with bright endosomes. Both dim and bright EEA1-positive endosomes take part in EGFR endocytosis, but bright endosomes interact with EGFR for longer time. In respect to method development, we plan to extend MrComas for processing of 3D image stacks.



## Acknowledgment

Experiments and quantitative analysis of the EEA1 vesicle subpopulations were supported by the RSF Grant No.14-50-00068 and the Federal Agency of Scientific Organizations (Russia). Development of the MrComas algorithm, evaluation of its performance and comparison with other segmentation methods was supported by the RSF Grant No. 14-14-00302. Imaging was supported by RRC MCT SPbSU. We thank Dr. Alexander Kanapin and Dr. Svetlana Surkova for comments and valuable advises.

## References

1. Aguet F, Antonescu C, Mettlen M, Schmid S, Danuser G, Advances in analysis of low signal-to-noise images link dynamin and ap2 to the functions of an endocytic checkpoint, *Dev Cell* **26**:279–291, 2013.
2. Barbieri MA, Kong C, Chen PI, Horazdovsky BF, Stahl PD, The src homology 2 domain of rin1 mediates its binding to the epidermal growth factor receptor and regulates receptor endocytosis, *J Biol Chem* **278**(34):32027–32036, 2003.
3. Bolte S, Cordelières FP, A guided tour into subcellular colocalization analysis in light microscopy, *J Microsc* **224**(3):213–232, 2006.
4. Boykov Y, Kolmogorov V, An experimental comparison of min-cut/max-flow algorithms for energy minimization in vision, *IEEE Trans Pattern Anal Mach Intell* **26**(9):1124–1137, 2004.
5. Caselles V, Kimmel R, Sapiro G, Geodesic active contours, *Int J Comput Vis* **22**(1):61–79, 1997.
6. Chang H, Yang Q, Parvin B, Segmentation of heterogeneous blob objects through voting and level set formulation, *Pattern Recognit Lett* **28**(13):1781–1787, 2007.
7. Collinet C, Stoter M, Bradshaw CR, Samusik N, Rink JC, Kenski D, Habermann B, Buchholz F, Henschel R, Mueller MS, Nagel WE, Fava E, Kalaidzidis Y, Zerial M, Systems survey of endocytosis by multiparametric image analysis, *Nature* **464**(7286):243–249, 2010.
8. Costes SV, Daelemans D, Cho EH, Dobbin Z, Pavlakakis G, Lockett S, Automatic and quantitative measurement of protein–protein colocalization in live cells, *Biophys J* **86**(6):3993–4003, 2004.
9. Crimmins TR, Geometric filter for speckle reduction, *Appl Opt* **24**:1438–1443, 1985.
10. de Chaumont F, Dallongeville S, Chenouard N, Herve N, Pop S, Provoost T, Meas-Yedid V, Pankajakshan P, Lecomte T, Le Montagner Y, Lagache T, Dufour A, Olivo-Marin JC, Icy: An open bioimage informatics platform for extended reproducible research, *Nat Meth* **9**(7):690–696, 2012.
11. Dufour A, Meas-Yedid V, Grassart A, Olivo-Marin JC, Automated quantification of cell endocytosis using active contours and wavelets, *19th Int Conf Pattern Recognition, 2008. ICPR 2008*, pp. 1–4, 2008.
12. Dunn KW, Kamocka MM, McDonald JH, A practical guide to evaluating colocalization in biological microscopy, *Am J Physiol Cell Physiol* **300**(4):C723–C742, 2011.
13. Eliceiri KW, Berthold MR, Goldberg IG, Ibanez L, Manjunath BS, Martone ME, Murphy RF, Peng H, Plant AL, Roysam B, Stuurman N, Swedlow JR, Tomancak P, Carpenter AE, Biological imaging software tools, *Nat Meth* **9**:697–710, 2012.
14. Helmuth J, Burckhardt C, Greber U, Sbalzarini I, Shape reconstruction of subcellular structures from live cell fluorescence microscopy images, *J Struct Biol* **167**(1):1–10, 2009.

15. Huang F, Kirkpatrick D, Jiang X, Gygi S, Sorkin A, Differential regulation of EGF receptor internalization and degradation by multiubiquitination within the kinase domain, *Mol Cell* **21**(6):737–748, 2006.
16. Inoue H, Matsuzaki Y, Tanaka A, Hosoi K, Ichimura K, Arasaki K, Wakana Y, Asano K, Tanaka M, Okuzaki D, Yamamoto A, Tani K, Tagaya M,  $\gamma$ -SNAP stimulates disassembly of endosomal snare complexes and regulates endocytic trafficking pathways, *J Cell Sci* **128**(15):2781–2794, 2015.
17. Kozlov K, Pisarev A, Kaandorp J, Samsonova M, Prostack, An image analysis software for identification and quantification of objects visualized with microscope, *Abstract Book of The 9th Int. Conf. Syst Biol*, Goteborg, p. 191, 2008.
18. Kramer HP, Bruckner JB, Iterations of a non-linear transformation for enhancement of digital images, *Pattern Recognit* **7**(12):53–58, 1975.
19. Manders EMM, Verbeek FJ, Aten JA, Measurement of co-localization of objects in dual-colour confocal images, *J Microsc* **169**(3):375–382, 1993.
20. Meyer F, Topographic distance and watershed lines, *Signal Process* **38**(1):113–125, 1994.
21. Murphy RF, Maturation models for endosome and lysosome biogenesis, *Trends Cell Biol* **1**(4):77–82, 1991.
22. Otsu N, A Threshold selection method from gray-level histograms, *IEEE Trans Syst Man Cybern* **1**:62–66, 1979.
23. Pham TD, Crane DI, Tran TH, Nguyen TH, Extraction of fluorescent cell puncta by adaptive fuzzy segmentation, *Bioinf* **20**(14):2189–2196, 2004.
24. Ridler T, Calvard S, Picture Thresholding using an iterative selection method, *IEEE Trans Syst Man and Cybern* **8**(8):630–632, 1978.
25. Rink J, Ghigo E, Kalaidzidis Y, Zerial M, Rab conversion as a mechanism of progression from early to late endosomes, *Cell* **122**(5):735–749, 2005.
26. Rizk A, Paul G, Incardona P, Bugarski M, Mansouri M, Niemann A, Ziegler U, Berger P, Sbalzarini IF, Segmentation and quantification of subcellular structures in fluorescence microscopy images using squash, *Nat Protoc* **9**:586–596, 2014.
27. Schneider CA, Rasband WS, Eliceiri KW, Nih image to imagej: 25 years of image analysis, *Nat Meth* **9**(7):671–675, 2012.
28. Serra J, Vincent L, An overview of morphological filtering, *Circuits Syst Signal Process* **11**(1):47–108, 1992.
29. Simonsen A, Lippe R, Christoforidis S, Gaullier JM, Brech A, Callaghan J, Toh BH, Murphy C, Zerial M, Stenmark H, Eea1 links pi(3)k function to rab5 regulation of endosome fusion, *Nature* **394**:494–498, 1998.
30. Stenmark H, Aasland R, Toh BH, D'Arrigo A, Endosomal localization of the autoantigen EEA1 is mediated by a zinc-binding FYVE finger, *J Biol Chem* **271**(39):24048–24054, 1996.
31. Tonti S, Cataldo SD, Bottino A, Ficarra E, An automated approach to the segmentation of hep-2 cells for the indirect immunofluorescence ANA test, *Comput Med Imaging Graph* **40**:62–69, 2015.
32. Velasco-Forero S, Angulo J, Soille P, Conditional toggle mappings: Principles and applications, *J Math Imaging Vis* **48**(3):544–565, 2014.
33. Vincent L, Morphological grayscale reconstruction in image analysis: Applications and efficient algorithms, *IEEE Trans Image Process* **176**–201, 1993.
34. Xu N, Ahuja N, Bansal R, Object segmentation using graph cuts based active contours, *Comput Vis Image Underst* **107**(3):210–224, 2007.
35. Zlobina MV, Kamentseva RS, Kornilova ES, Kharchenko MV, Analysis of vesicle subpopulations carrying early endosomal autoantigene EEA1, *Tsitologiya* **10**:741–749, 2014.

**Dr. Konstantin Kozlov** graduated from the Peter the Great St. Petersburg Polytechnic University, one of the top-rated universities in Russia, and obtained the Ph.D. degree in Bioinformatics, Computational biology and Modeling in 2013. He has been a research fellow in the Mathematical Biology and Bioinformatics Lab since 2001 and became a leading researcher in 2014. Dr. Kozlov is a specialist in Applied Mathematical Methods and Information Technologies, and conducts scientific research in the field of Mathematical Modeling of Biological Systems, Optimization and Biomedical Image Processing.

**Vera Kosheverova** earned her Master's degree from the Faculty of Biology, Saint Petersburg State University, and her postgraduate course is nearly under completion. She is currently a research fellow in the Laboratory of Intracellular Membrane Dynamics, Institute of Cytology, St. Petersburg. Her research interests concern the investigation of the early endocytic pathway organization in mammalian cells.

**Rimma Kamentseva** obtained her Master's degree from the Faculty of Biology, Saint Petersburg State University. She is currently a Ph.D. student at the Institute of Cytology RAS under the supervision of Prof. Elena Kornilova. Her research interests are focused on endocytosis regulation and image analysis.

**Dr. Marianna Kharchenko** obtained her Master's degree from the Faculty of Biology, St. Petersburg State University, and her Ph.D. in Cell Biology from Institute of Cytology RAS. Now she is a staff researcher at the Institute of Cytology. Her current research is focused on vesicular trafficking and cytoskeleton organization in mammalian cells.

**Alena Sokolkova** obtained her Master's degree from the Peter the Great St. Petersburg Polytechnic University. She is currently a research fellow in the Mathematical Biology and Bioinformatics Laboratory. Her research interests include Biomedical Image Processing and Computational Biology.

**Prof. Elena Kornilova** is a Head of the Laboratory of Intracellular Membrane Dynamics, Institute of Cytology RAS, St. Petersburg. She is also a Professor at the Department of Medical Physics of Polytechnical University, St. Petersburg. Her main research areas are vesicular traffic and intracellular signalization.

**Prof. Dr. Maria Samsonova** is the head of Mathematical Biology and Bioinformatics Laboratory at the Peter the Great St. Petersburg Polytechnic University. She has expertized in mathematical modeling of complex biological systems and develops several models of segment determination dynamics in fruit fly *Drosophila*. These models based on non-linear discrete or partial differential equations were used in both the interpretive and predictive modes to already obtain several results of significant biological interest.